13 Cosmic Rays and the Earth

Vladimir Mares, Werner Rühm, Helmholtz Center Munich, Institute of Radiation Medicine

Abstract

The Earth is constantly being bombarded with particles from the galactic space and from the Sun with energies that are sufficiently high to penetrate the geomagnetic shielding of the Earth. These high-energy particles, also called primary cosmic rays (CRs), do not reach ground level because they interact with atoms in the atmosphere and initiate air showers producing many secondary particles. Some of these particles, also called secondary CRs, reach the ground and can be detected. An important contribution of secondary CRs to radiation-induced health risks comes from neutrons, because they contribute up to about 60 % to the ambient dose equivalent, H*(10), from CRs at mountain regions.

The history of CR measurements can be traced back to the beginning of the 1910’s, when an Austrian-American physicist, Victor Franz Hess, started series of measurements with ionization chambers onboard balloons. Since the 1950’s, neutron monitors are considered as the best ground-based detectors for recording any variations of the primary CR intensity. However, a single neutron monitor does not provide any information on the energy distribution of detected neutrons. This knowledge is important, however, because it can help scientists to understand the nature of CRs. In 1997, major efforts have been made at the Helmholtz Zentrum München (former GSF) when the first ground-based measurement of the energy distribution of neutrons from secondary CRs with an extended-range Bonner sphere spectrometer were performed at the summit of Zugspitze mountain (2,963 m a.s.l.), Germany. Since 2005, the neutrons from secondary CRs have been continuously monitored with such a spectrometer at the Environmental Research Station Schneefernerhaus at Zugspitze (2,650 m a.s.l.).

The following section of this chapter summarizes general characteristics of CRs, and the three main kinds of shields protecting the Earth from CRs, namely the interplanetary magnetic field, the geomagnetic field, and the Earth’s atmosphere.

The next section deals with the definition of effective dose as a protection dose quantity used for the implementation of dose limits. Because effective dose cannot be measured in practice, ambient dose equivalent, H*(10), is described as an operational dose quantity used to quantify external radiation exposures.

The third section describes detection principles of the extended-range Bonner sphere spectrometer installed in an instrument shed at the Environmental Research Station Schneefernerhaus at Zugspitze. All steps necessary for the data evaluation process in terms of detector counts and neutron spectrometry are explained. Special consideration is given to air pressure correction of measured count rates, and to the unfolding process used to derive neutron fluence energy spectra from measured count rates.

In the last section, two examples of long-term measurements of neutrons from secondary CRs with one-hour time resolution are shown. First, a rapid decrease within a few hours in measured intensity of secondary CR neutrons, a so-called Forbush decrease, was recognized in the count rates measured in September 2005. Second, the effect of snow cover on the neutron fluence energy spectra at ground level was observed between January 2010 and June 2014. The hypothesis that the snow cover might influence the number of neutrons absorbed or backscattered from soil (so-called albedo neutrons) was tested with Monte Carlo simulations. Finally, seasonal oscillations in neutron fluence due to the presence of a snow cover in winter and its absence in summer are described.

Keywords: Primary cosmic rays, secondary cosmic rays, neutron spectrometry, dose rate from cosmic rays

13.1 Cosmic Rays at the Surface of the Earth

The Earth is continuously exposed to high-energy particles from the galactic space (“galactic cosmic rays” – GCRs) and occasionally also from the Sun (“solar cosmic rays” – SCRs). These cosmic ray particles travel with almost the speed of light. When these particles, often called “primary cosmic rays”, enter the Earth’s atmosphere they interact with the atoms there. From the interactions with the atmospheric nuclei, a complex field of secondary particles is formed which are often called “secondary cosmic rays”. In general, cosmic rays contribute to the radiation exposure of the population. A general introduction on cosmic rays can be found in (Grieder 2001).

13.1.1 Primary Cosmic Rays

13.1.1.1 Galactic Cosmic Rays and Shielding by the Interplanetary Magnetic Field

Galactic Cosmic Rays consist mainly (i. e., about 98 %) of hydrogen and helium nuclei (protons and alpha particles), but heavier nuclei, electrons, positrons and other components can also be found. When charged particles enter the solar system (heliosphere), they are deflected by the interplanetary magnetic field of the Sun (Lorentz force[1]). Therefore, the intensity of the GCR particles entering into the inner heliosphere is attenuated. As the magnetic field of the Sun is correlated with the activity of the Sun, the attenuation of the GCR intensity is not constant with time. During periods of higher solar activity the GCR intensity near Earth is lower, and higher during periods of lower solar activity, i. e. the intensity of GCR particles close to the Earth’s orbit is anti-correlated with the 11-years cycle of the solar activity, which can be quantified by the Sunspot number.

Except for this 11-years cycle, the intensity of GCR particles entering the solar system is fairly constant with time. As a further exception, their intensity near the Earth may decrease for hours or days (“Forbush decrease”[2]), following a large coronal mass ejection (CME) from the Sun’s corona which causes changes in the interplanetary magnetic field.

Particles of GCR can have energies up to 10^{20} eV[3], but lower-energy particles are the most frequent. After the GCR particles have penetrated the interplanetary magnetic field of the solar system, they approach the Earth rather isotropically. The peak of their energy spectrum close to the Earth’s orbit is at a few hundred MeV to 1 GeV per nucleon.

13.1.1.2 Solar Cosmic Rays

The Earth is occasionally also exposed to energetic protons and heavier particles that are accelerated in high-energy processes at or near the Sun (reconnection of magnetic field lines, shock waves from CMEs). When a CME is directed towards the Earth, it can disturb the geomagnetic field (geomagnetic storm) a few days after its release from the Sun. The energy spectrum of solar particle events (sometimes also called “solar proton events”, both abbreviated by “SPEs”) is less energetic than the GCR energy spectrum. Generally, the maximum energy of solar particles is below 100 MeV and only rarely above 10 GeV. SPEs are of short duration, a few hours to a few days, and highly variable in intensity. The frequency of SPEs is roughly correlated with the 11-year solar activity cycle. SPEs are most prevalent during the years around solar maximum (Shea and Smart, 2000; Feynman et al., 1993, Shea and Smart, 1990, 1999), but significant solar particle events have also occurred during solar minimum. Only a small fraction of SPEs, on average one per year, includes particles with energies high enough to produce secondary particles in the atmosphere that are able to reach the surface of the Earth. Such events are called ground level enhancements (GLEs).

Additionally, there is the solar wind, a stream of charged particles (called solar-wind plasma) released from the Sun’s corona. This plasma consists mostly of electrons, protons, and alpha

---

[1] Hendrik A. Lorentz (1853–1928), Dutch physicist, Nobel Prize in 1902.

[2] Scott E. Forbush (1904–1984), American astronomer, physicist and geophysicist.

[3] eV is a physical unit of energy; in SI units it corresponds approximately to 1.6×10^{-19} joule (J). One eV is the energy gained or lost by an electron (having the elementary charge of 1.6×10^{-19} C) moving along an electric potential difference of 1 volt (V).

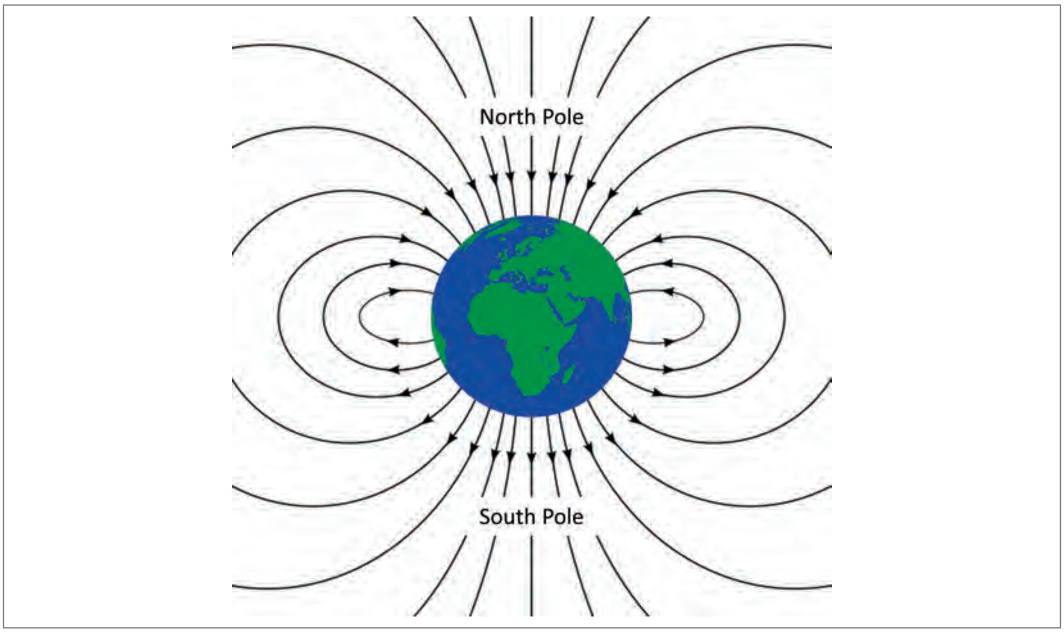

Fig. 1: Sketch of the geomagnetic field

particles. The interplanetary magnetic field is embedded within the solar-wind plasma. The solar wind varies in density, temperature and speed over time and depends on solar latitude and longitude. Its particles can escape the Sun's gravity because of their high energy resulting from the high temperature of the corona.

The Earth is protected against the solar wind by the geo-magnetic field, which deflects the charged particles of the solar wind (see below). Some of the charged particles are, however, trapped in the Van Allen radiation belts, and a smaller number of particles can travel to the Earth's upper atmosphere and ionosphere in the aurora zone. The solar wind is observable on the Earth when it is strong enough to produce phenomena such as the "Aurora borealis" above the north magnetic pole and "Aurora australis" above the south magnetic pole.

13.1.1.3 Geomagnetic Shielding

The Earth is shielded against the galactic and the solar cosmic rays by the Earth's magnetic field ("geomagnetic field"), as charged particles are deflected in a magnetic field by the Lorentz force. The shielding by the geomagnetic field is most effective at low geomagnetic latitudes (i. e., close to the geomagnetic equator), and less effective at high geomagnetic latitudes (i. e., close to the geomagnetic poles). This is so because near the equator the trajectories of cosmic ray particles are mainly perpendicular to the geo-magnetic field lines resulting in a strong Lorentz force. In contrast, the trajectories close to the magnetic poles are rather parallel to the magnetic field lines and, accordingly, the Lorentz force becomes weaker.

13.1.2 Secondary Cosmic Rays

Particles of the primary cosmic rays may interact with the atomic nuclei of atmospheric elements (e. g., oxygen, nitrogen), and the number of interactions depends on energy and intensity of the primary particles. These interactions lead to a variety of secondary particles including for example protons, neutrons, electrons, positrons, photons, muons (positive and negative), and pions (positive and negative). The energy of these particles covers many orders of magnitude and depends on the particle type. For example, the energy of secondary neutrons ranges from thermal energies (several meV or tens of meV) up to about 10 GeV. Due to the competing processes of secondary particle production and absorption in the atmosphere, the number of SCR particles is increasing with increasing height above the Earth's surface up to the Pfotzer Maximum at an altitude of about 15–20 km.

13.1.3 Surface and Near-Surface Observations of Cosmic Rays

Because the intensity of the GCR depends on the interplanetary solar magnetic field which in turn depends on the solar activity (see chapter 13.1.1), the production of secondary cosmic rays in the atmosphere also depends on the solar activity. Fig. 2 shows the number of counts measured at the surface of the Earth by a so-called neutron monitor, due to neutrons from secondary cosmic rays. Clearly, during the measurement period of 50 years corresponding to about five cycles of solar activity, the reading of this instrument showed an anti-correlation with Sunspot number, which in turn is a measure for solar activity.

As also mentioned in Chapter 13.1.1, the magnetic field of the Earth also shields against impinging charged particles. For this reason, the production of SCR particles in the atmosphere depends on geomagnetic latitude and, consequently, the dose rate from cosmic rays at any point of interest in the atmosphere also depends on geomagnetic coordinates (for definition of dose quantities see chapter 13.2). This is demonstrated in Fig. 3 where the calculated effective dose rate due to GCRs at an altitude of 11.3 km above sea level in 2005 is shown. Due to the geomagnetic field, the effective dose rate is only about 2 μSv per hour close to the equator, while it is about 7 μSv per hour close to the magnetic North and South poles of the Earth.

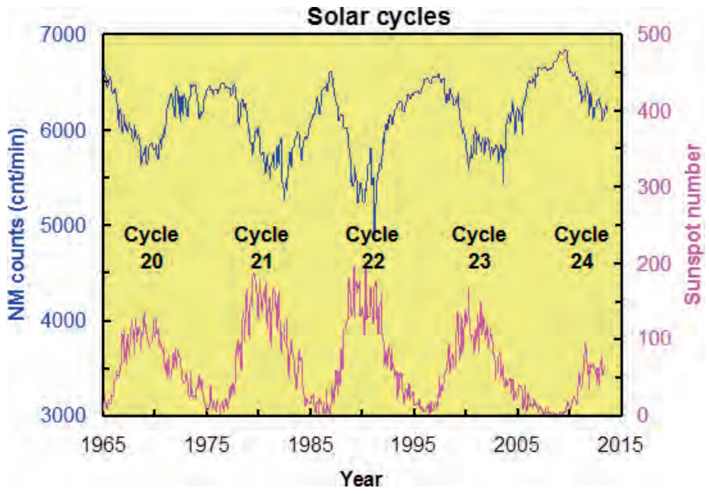

Fig. 2: Monthly averaged sunspot numbers (lower magenta curve) and counts measured by the Oulu Neutron Monitor (upper blue curve), for solar cycles 20 through 24 (Sunspots: from WDC-SILSO, Royal Observatory of Belgium, Brussels; Neutron monitor counts: from I. G. Usoskin and co-workers, http://cosmicrays.oulu.fi/

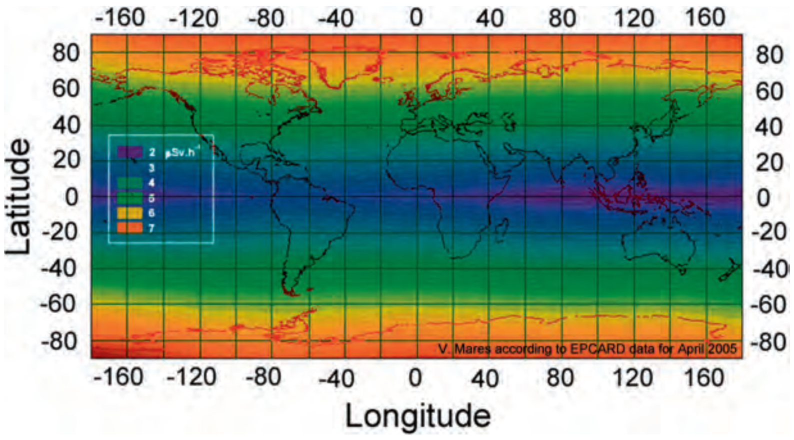

Fig. 3: World map of effective dose rate calculated with the EPCARD code for an altitude of 11.3 km above sea level and for April 2005 (Mares et al. 2009).

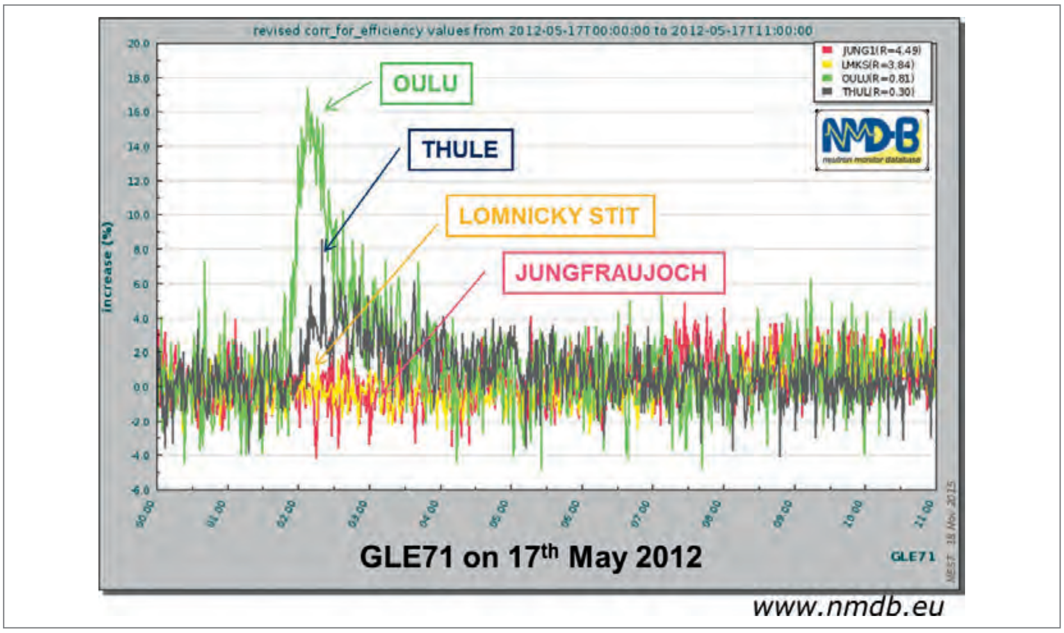

Fig. 4: Relative count rate increases as detected by several Neutron Monitors (at Oulu, Finland; Thule, Greenland; Junfraujoch, Switzerland, und Lomnicky Stit, Slovakia) during GLE71 on May 17, 2012 (Source: Neutron Monitor Data Base, www.nmdb.eu).

Ground level enhancements (GLEs, see above) can also be detected by ground based neutron monitors. Fig. 4 shows as an example, short-term increases in neutrons from secondary cosmic rays as detected by a number of neutron monitors during GLE71 which occurred on May 17, 2012. Due to the anisotropic nature of this event, and due to the different geo-magnetic shielding at the locations of the neutron monitors, the count rates measured by these neutron monitors are rather different.

13.2 Radiation Dose Quantities

In general terms, interaction of ionizing radiation with matter (either inorganic or organic in nature) may give rise to the absorption of energy in the irradiated material. This is often quantified in terms of absorbed dose per unit mass, *D*, which is expressed in SI units of J/kg, and the special name "gray"[4] was proposed by the International Commission on Radiological Protection, and the International Commission on Radiation Units and Measurements (ICRP 2007, ICRU 1993).

Although the absorbed dose might be a first indicator of radiation damage, for biological effects on organic materials additional factors are also important. For example, even for the same absorbed dose, different types of radiation (e. g., alpha, beta, gamma radiation, neutrons) can cause different biological effects. More specifically, neutrons, protons and alpha particles can cause 5–20 times more damage (e. g., chromosome aberrations in the cell nucleus) than the same absorbed dose of beta or gamma radiation. This is due to differences in the spatial distribution of the radiation-induced damage. In fact, ionizing events induced by neutrons or alpha particles of a certain energy in tissue are located much closer together than those induced by gamma radiation, resulting in more complex radiation damage which is more difficult for cells to repair.

13.2.1 Operational Dose Quantities

For this reason, in operational radiation protection the dose equivalent *H* defined by the product of the absorbed dose *D* at a point of interest in tissue and the radiation quality factor *Q* at this point was introduced by ICRU (Eq. 1):

---

[4] Lois H. Gray (1905–1965), English physicist

$$H = QD \quad (1)$$

where Q describes the biological effects depending on radiation type based on physical considerations by taking into account different ionisation densities. Because Q is without dimension, the unit of H is J/kg and the special name is sievert (Sv)[5].

The ambient dose equivalent, $H^*(10)$, is the operational quantity for area monitoring. It is the dose equivalent at a point in a radiation field that would be produced by the corresponding expanded and aligned field in a 30-cm-diameter sphere of unit density tissue (ICRU-sphere) at a depth of 10 mm on the radius vector opposing the direction of the aligned field (ICRU 1993).

13.2.2 Radiation Protection Dose Quantities

In contrast to ICRU, the ICRP has introduced the radiation weighting factor w_R based on experimental biological evidence (e. g., based on cellular and animal experiments) which, multiplied with absorbed dose, gives the equivalent dose, to account for the differences in biological effects induced by different radiation types. In addition, because it is well known that different human tissues (i. e., organs) react differently to radiation, ICRP has introduced tissue weighting factors, w_T. Accordingly, for routine radiation protection purposes ICRP recommends the use of the effective dose E, which is a rough indicator of the risk of stochastic effects (e. g., cancer, leukemia, hereditary effects) from ionizing radiation (ICRP 2007). E is defined as the tissue-weighted sum of the equivalent doses in all specified tissues and organs of the body, given by Eq. 2:

$$E = \sum_T w_T H_T = \sum_T w_T \sum_R w_R D_{T,R} \quad (2)$$

where H_T is the equivalent dose in a tissue or organ T given by $\sum_R w_R D_{T,R}$; $D_{T,R}$ is the mean absorbed dose from radiation type R in a tissue or organ T, and w_R and w_T are the radiation and tissue weighting factors, respectively. The SI unit for the effective dose is joule per kilogram ($\mathrm{J\,kg^{-1}}$) and its special name is sievert (Sv).

13.3 Measurement of Neutrons from Secondary Cosmic Rays – the Extended-Range Bonner Sphere Spectrometer

13.3.1 Detection Principle

The original Bonner sphere spectrometer (BSS) was first described in 1960 by Bramblett, Ewing and Bonner (Bramblett et al., 1960). It is a device used to determine the energy spectrum of neutrons from thermal energies up to about 20 MeV. It employs thermal neutron detectors embedded in polyethylene (PE) moderating spheres of different sizes. In an effort to increase the BSS response for high-energy neutrons above 20 MeV up to 1 GeV, the HMGU BSS has been modified by adding two 9 inch spheres that include lead shells of different thickness (0.5 and 1 inch) [Mares et al., 1998a]. This device is called here Extended-Range Bonner Sphere Spectrometer (ERBSS). The HMGU ERBSS with 16 measuring channels uses 16 ^{3}He gas-filled spherical proportional counters of 3.3 cm diameter with partial pressure of 172 kPa (type SP9, Centronic Ltd.) and 13 PE spheres of different diameters (2.5, 3, 4, 5, 5.5, 6, 7, 8, 9, 10, 11, 12, 15 inch). One ^{3}He proportional counter without any PE sphere is used to measure thermal neutrons (Fig. 5). The SP9 ^{3}He detectors operate within the proportional region at a voltage of +800 V. The signals from these SP9 detectors are amplified in ACHEM7E charge sensitive preamplifiers and a Multiport II, both produced by Canberra Industries Inc. After that a built-in ADC (analog-to-digital converter) converts the amplified analog signals into digital signals.

---

[5] Rolf M. Sievert (1896–1966), Swedish medical physicist

Fig. 5: The HMGU Extended-Range Bonner Spheres Spectrometer (ERBSS): left – ^{3}He gas-filled spherical proportional counter; middle – polyethylene sphere with lead shell; right – ERBSS at the UFS – PE spheres of various sizes surround the ^{3}He counters.

^{3}He filled proportional counters are most suitable for the detection of thermal neutrons because of their high neutron capture cross-section ($\sigma_{n,\,th}$ = 5.330 b) for the (n, p) nuclear reaction: after capture of a neutron by a ^{3}He nucleus, a proton is emitted and a ^{3}H (triton) nucleus is left. The kinetic energies of proton and triton are 573 and 192 keV, respectively, sharing the reaction energy of 764 keV plus the kinetic energy of the incident neutron. Both the proton and the triton are charged ions that lose their energy in the ^{3}He counter gas, producing ionizations along the proton and triton tracks and creating pulses with amplitudes that are proportional to the proton and triton energies.

The pulse-height spectrum measured by a ^{3}He proportional counter is quite complex. Depending on the counter dimension and ^{3}He pressure, the maximum track lengths of the proton and triton ions may be larger than the geometric dimensions of the counter. This results in pulses with reduced amplitudes and generates a continuous spectrum with two steps at 192 keV and 573 keV, respectively. It is only when both particles are stopped within the sensitive volume of the counter, that the height of the resulting current pulse is proportional to 764 keV. An example of a pulse-height distribution from an SP9 operating at a partial pressure of 172 kPa is shown in Fig. 6.

For each of the SP9 counters used, the counts between the left and right boundaries of region of interest (ROI) are added up (see Fig. 6) and divided by the measurement time (in seconds) to get the counts per second (“count rate”) shown in Fig. 7.

Once the count rates obtained by the measurement channels are known, conversion factors are needed to calculate neutron fluences from the count rates. For this, the fluence response functions HEMA99 of all spheres with a ^{3}He proportional counter in their center were calculat-

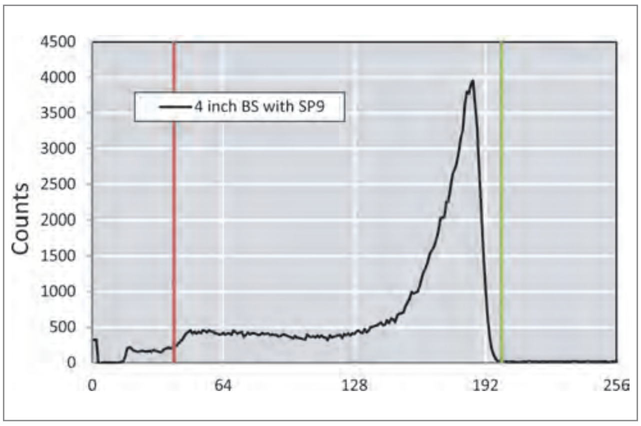

Fig. 6: Pulse height spectrum obtained with an SP9 ^{3}He proportional counter placed inside of 4 inch Bonner sphere: red and green vertical lines – define the region of interest (ROI). x-axis: channel numbers

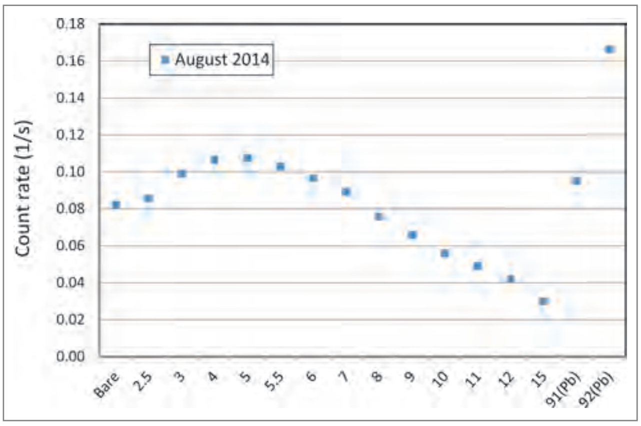

Fig. 7: Mean count rates measured in August 2014 on the UFS by means of the ERBSS. Data are corrected for a reference air pressure of 740 mbar.

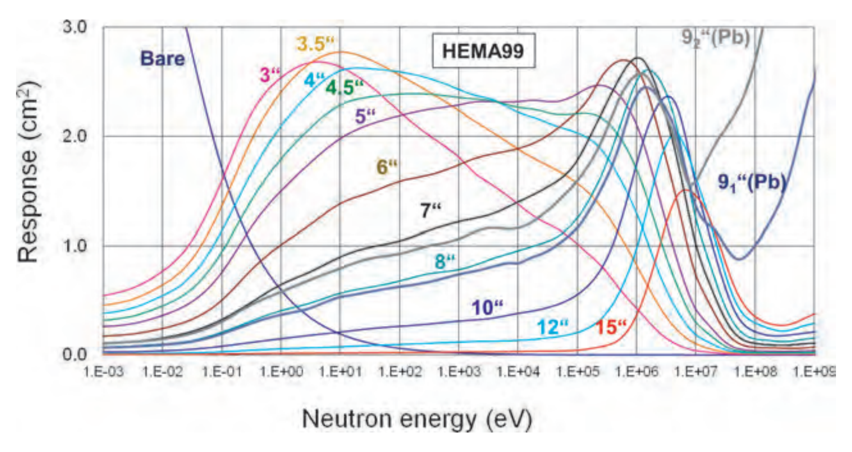

Fig. 8: Response functions of HMGU ERBSS calculated by Monte Carlo simulations as a function of neutron energy (Mares et al. 1991, 1998b).

ed by means of Monte Carlo (MC) simulations (Mares et al. 1991, 1998b) and experimentally validated at 13 mono-energetic neutron energies between thermal energies and 14.8 MeV (Alevra et al. 1992; Thomas et al. 1994), as well as at quasi-mono-energetic neutron fields with peak energies at 244 MeV and 387 MeV (Mares et al. 2013) (see Fig. 8). In the figure, response denotes the number of counts detected relative to the number of impinging neutrons per cm^2.

13.3.2 Unfolding

The most complex part of neutron spectrometry is the unfolding process. Neutron energy spectra can be derived by unfolding the ERBSS neutron detector readout, i.e., the count rates provided by M ^{3}He proportional counters of the ERBSS. The count rate measured by the j_{th} detector, C_j, is given by a Fredholm integral equation of the first kind, where $R_j(E)$ is the response function of the j_{th} detector and $\Phi(E)$ the neutron fluence to which the system is exposed (Eq. 3).

$$C_j = \int_{E_{min}}^{E_{max}} R_j(E)\,\Phi(E)\,dE \qquad j = 1,2,\ldots,M \tag{3}$$

To obtain a numerical solution, the system of Eqs. 3 is usually rewritten in terms of a discrete system of equations, described by Eq. 4, where $R_j(E_k)$ is the response function of the j_{th} sphere to neutrons of the energy that corresponds to the k_{th} energy bin, N the number of energy bins and $\Phi(E_k)$ the fluence in the k_{th} energy bin. However, Eq. 4 has no unique solution, because the number of unknowns ($N = 130$ energy bins of fluence $\Phi(E)$) is usually much larger than the number of equations ($M = 16$ measuring channels), i.e., $N >> M$.

$$C_j = \sum_{k=1}^{N} R_j(E_k)\,\Phi(E_k) \qquad j = 1,2,\ldots,M \tag{4}$$

For this reason, the unfolding process must necessarily include some physical pre-information in addition to the simulated response functions, the measured count rates and their uncertainties. An initial (guess, *a priori*) neutron fluence spectrum containing physical information about the neutron field is a way to provide such a pre-information.

There are a number of unfolding codes based on different approaches that can be used to determine Φ(E) values that satisfy the system of equations formulated in Eq 4. For example, methods based on linear and non-linear least-squares methods, Bayesian methods, maximum entropy and artificial neural networks methods, among others, have been used (Reginatto et al. 2010). Typically, the UFS neutron spectra are unfolded from the ERBSS count rates by means of the MSANDB (Matzke 1987, 2002) unfolding code, which is based on the earlier SAND-II code (McElroy et al. 1967). MSANDB uses iterative procedures and requires an initial *a priori* spectrum. For more details see (Simmer et al. 2010).

13.3.3 Correction for Air Pressure

Because the absorption properties of the atmosphere with respect to cosmic rays depends on atmospheric density, air pressure is an important parameter that influences the intensity of secondary cosmic rays at the Earth's surface. Thus, the count rates measured by the ERBSS must be corrected for any changes in air pressure. Generally, data on meteorological parameters measured at the UFS are provided by the German Weather Service (DWD). Additionally, the air pressure and temperature are also measured continuously inside the HMGU measurement shed where the HMGU ERBSS is located (see Fig. 9).

Such data on air pressure were used to correct the count rates measured with the ERBSS, by means of Eq. 5. This is of particular importance if the influence of other environmental parameters are to be studied or if data of different research stations are to be compared.

$$N_{cor} = N \cdot \exp\left[-\beta \cdot (P_0 - P)\right] \tag{5}$$

Where N is the observed count rate at a particular pressure, P, and N_{cor} is the corrected value for a standard pressure, P_0 , of 740 mbar (Röhrs, 1995). The quantity β is a barometric coefficient and a value of 0.721 % per mbar was used.

Fig. 10 shows the un-corrected and pressure-corrected ERBSS count rates obtained from 24th March to 13th April 2015 for selected spheres. After pressure correction, the count rates are lower from 24th March to 4th April, because the air pressure during this period of time was below the reference pressure of 740 mbar (see Fig. 9). In contrast, because the air pressure values were close to 740 mbar during the period from 8th April to 13th April, the raw and corrected count rates are very similar for this time period.

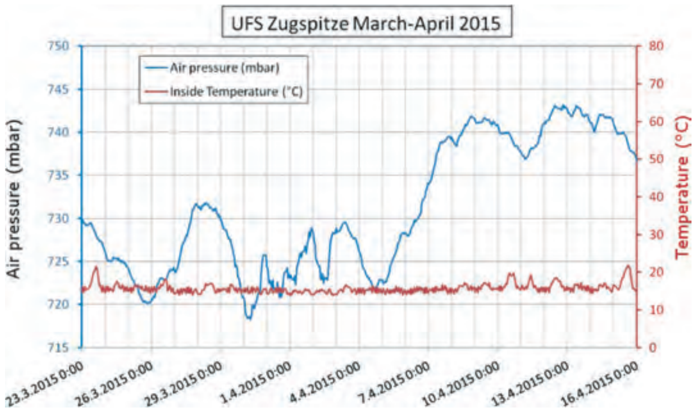

Fig. 9: Air pressure and temperature measured in March/April 2015 inside the HMGU instrument shed where the HMGU ERBSS is located.

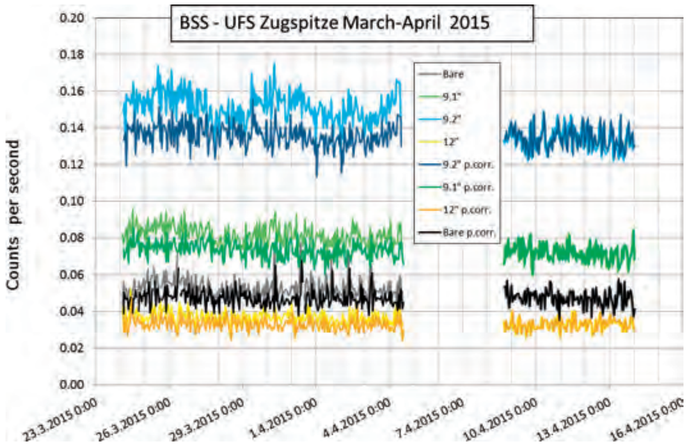

Fig. 10: Hourly un-corrected count rates as provided by selected ERBSS detectors in March/April 2015 (light colored lines), and pressure-corrected count rates at 740 mbar (dark-colored lines); the corresponding air pressure data are shown in Fig. 9.

13.3.4 The Extended-Range Bonner Sphere Spectrometer at the UFS

Fig. 11: Instrument shed on the measurement terrace of the UFS housing the Extended-Range Bonner Spheres Spectrometer of the HMGU (see also Fig. 5).

This HMGU ERBSS has been installed in 2004 at the Environmental Research Station "UFS Schneefernerhaus" (2,650 m above sea level) close to the summit of the Zugspitze Mountain, Germany, to measure continuously the energy spectrum of neutrons from secondary cosmic rays. Since October 2005, the system is running inside an instrument shed with slant roof on the terrace of the station (Figs. 5, 11) (Leuthold et al. 2009). The roof is tilted to avoid snow cover during winter times that could affect the measurements. Since then the ERBSS is providing routine data allowing the quantification of any variations in the intensity of neutrons from secondary cosmic rays, in the whole neutron energy range from a few meV up to GeV, larger than 10 %. A similar system is operating at the Koldewey station of the Alfred Wegener Institute, the French-German arctic polar base (Rühm et al. 2009a, 2009b).

13.4 Results 1: Forbush Decrease on 11th September 2005

A Forbush decrease (FD), named after the American physicist Scott E. Forbush, is a rapid decrease in GCR intensity within a few hours, due to the magnetic field of the solar-wind plasma sweeping some of the GCR particles away from Earth, followed by a more gradual recovery phase typically lasting for several days. An FD occurs after a coronal mass ejection (CME). The magnitude of an FD varies from a few percent up to 25 % in the decrease of GCR intensity. Such rapid changes in GCR intensity can for example be measured by neutron monitors (NMs).

Fig. 12 shows ERBSS count rates measured at the UFS Zugspitze in September 2005. The count rates obtained from all 16 ERBSS detectors were added, to reduce the statistical uncertainty, and compared to data from the neutron monitor on the Lomnicky Stit mountain (latitude: N 49° 20′, longitude: E 20° 22′, cutoff 3.84 GV, altitude 2,634 m), Slovakia. It is evident from Fig. 12 that a significant decrease was observed within a few hours in the morning of September 11th, which is attributed to a Forbush decrease. It is important to note that the second count rate decrease observed for a short period of time between the 17th and 20th of September was due to variations of environmental conditions (mainly snow cover; see below).

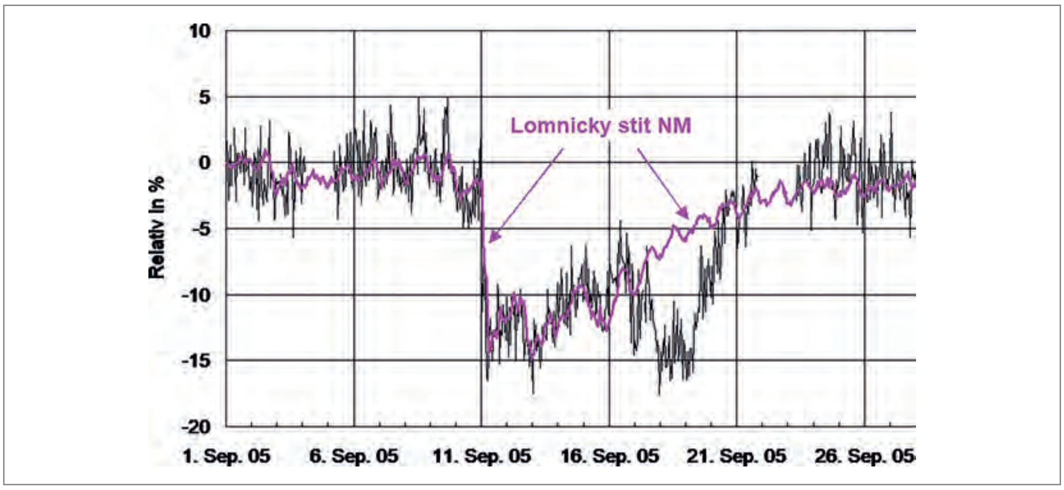

Fig. 12: Relative deviation of added hourly ERBSS count rates as measured in September 2005 (black line) compared to those measured by the Neutron Monitor at Lomnicky Stit, Slovakia (magenta line) (Leuthold et al., 2007).

13.5 Results 2: Influence of the Environment on Neutrons from Cosmic Rays

13.5.1 Effect of Snow – First Observations Based on Detector Count Rates

As already indicated earlier, the count rates obtained by the individual detectors of the ERBSS reflect the presence of neutrons from secondary cosmic rays, and the moderator thickness (i. e., radius of PE spheres) determines the energy range of these neutrons. For example, the count rates of the bare detector reflect the presence of thermal neutrons, while the count rates of the 9 inch spheres including lead mainly reflect the presence of high-energy neutrons. Fig. 13 shows, as an example, the monthly count rates of eight detectors (bare, 4”, 5”, 10”, 12”, 15’, 9-1”(Pb), and 9-2”(Pb)) obtained between January 2010 and June 2014. In the figure all count rates are normalized to a reference pressure of 740 mbar. Clearly, seasonal variations are visible suggesting the presence of less neutrons during winter times and more neutrons during summer times, which could be due to variations in snow cover.

In order to investigate this hypothesis, let us first have a look at an obvious short-term decrease in count rates observed in Fig. 13 during autumn 2011 (marked in red in the figure). The period between May and December 2011 was rather dry, but was interrupted by a short period of heavy snow fall early October of that year (see Fig. 14). Obviously, the increase of snow cover thickness in the vicinity of the UFS early October led to a decrease in detector counts, while during the following snow melt later in October the count rates of all detectors recovered.

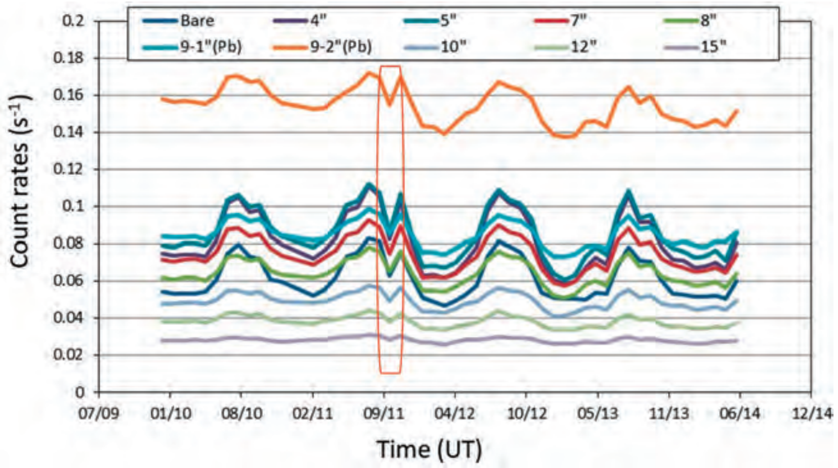

Fig. 13: Monthly count rates from eight detectors of the ERBSS, from Jan 2010 to June 2014, and normalized to a reference air pressure of 740 mbar. In autumn 2011 a short-term decrease in count rates can be observed (marked in red).

Fig. 14: UFS in September 2011 at dry conditions (left), and after heavy snow-fall in October 2011 (right).

13.5.2 Effect of Snow – Creation of a Hypothesis and First Simulations

The effect observed could be explained by the fact that a large part of the neutron spectrum measured at the UFS is from neutrons that were initially of very high energy, moderated in the ground towards lower energies, and then backscattered to the air where they were detected by the spectrometer. Any snow cover on top of the soil might absorb part of the backscattered neutrons ("albedo neutrons"), and the resulting neutron fluence above ground is reduced. Indeed, such an effect can be tested by Monte Carlo simulations.

Such simulates were performed by the GEANT4 code, which was initially developed at CERN to simulate the efficiency of various instruments to detect high-energy particles. In the present example, the code was used to simulate the transport of particles of secondary cosmic rays in an atmospheric volume of $100 \times 100 \times 317\ m^3$, allowing for moderation in and backscattering from soil. It was assumed that secondary neutrons impinge perpendicularly on that air volume (i.e., at a height of 317 m above ground) with an energy distribution as given by Roesler and co-workers (Roesler et al. 2002). Backscattered neutrons were scored at a height of 150 cm and averaged over an area of $20 \times 20\ m^2$. Although these assumptions represent only a simplified model of the real situation (for example, the angular distribution of impinging neutrons was neglected, the ground at the UFS is not horizontal but tilted, the UFS building and the measurement terrace with the ERBSS instrument was not modelled, etc.), they are useful to demonstrate the effect of snow cover on backscattered neutrons from secondary cosmic rays. Fig. 15 shows the energy distribution of neutrons backscattered from soil with a typical elemental composition without any snow or water on top. Dominating are neutrons between 20 and 500 MeV in energy ("cascade neutrons") and those between 400 keV and 20 MeV ("evaporation neutrons"), and neutrons between 200 meV and 200 keV ("epithermal neutrons"). The presence of a water layer of 50 cm in the simulation covering the soil changes the situation: while almost no effect can be seen at high energies, the number of neutrons below 20 MeV is significantly reduced (a similar effect is seen for a water layer of 100 cm). Note that, for typical snow densities, a water layer of 50 cm might correspond to a snow layer of 100–150 cm thickness.

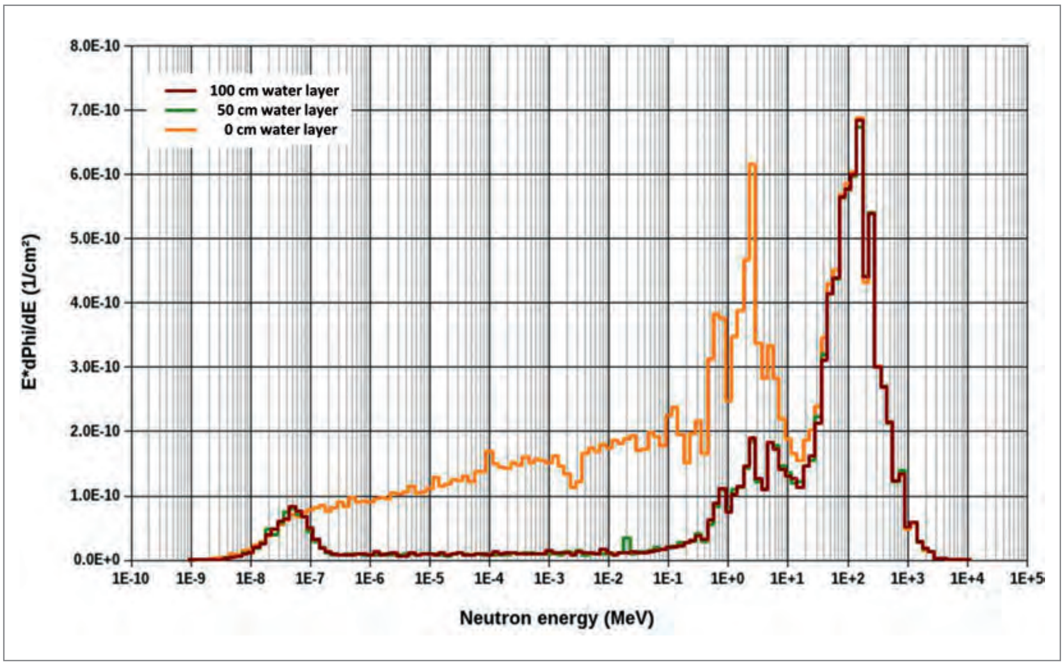

Fig. 15: Neutron spectra simulated with the Monte Carlo code GEANT4 at a height of 150 cm above ground, covered by water layers of various thickness (0 cm, 50 cm and 100 cm) (S. Trinkl, private communication, 2014).

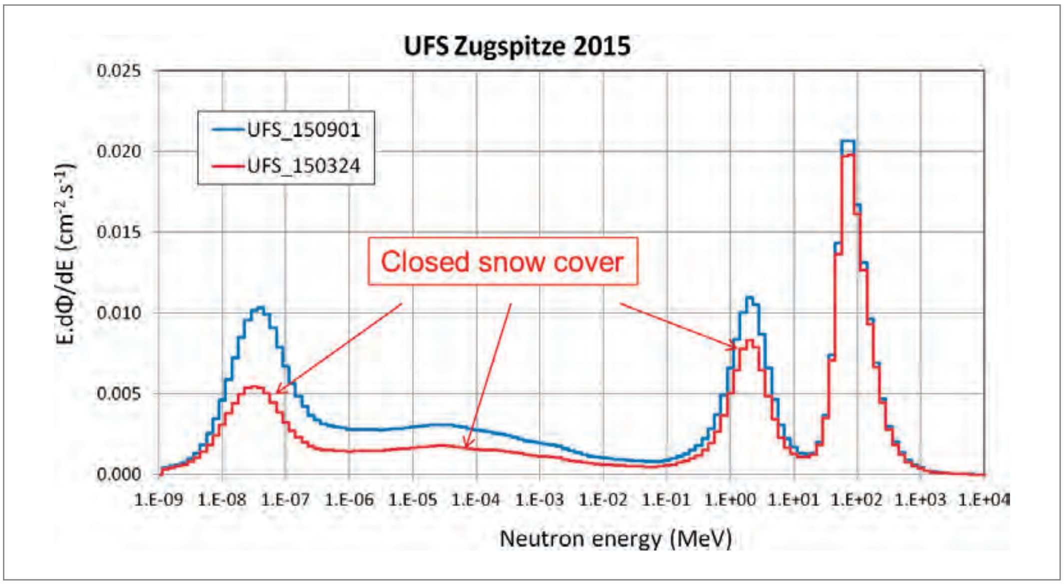

Fig. 16: Neutrons of secondary cosmic rays measured with the ERBSS on September 2015 (blue curve) and March 2015 (red curve).

13.5.3 Effect of Snow – Influence on Neutron Energy Distribution

In order to investigate the influence of environmental parameters under real conditions experimentally, we unfolded the count rates obtained by the ERBSS (see above) during dry periods and during periods with heavy snow cover. In Fig. 16 this was for example done for March 2015 (heavy snow cover) and September 2015 (no snow in the vicinity of the UFS). As expected, the high-energy cascade neutrons were not affected by the presence of snow. In contrast, neutrons with an energy of less than 20 MeV were reduced, as was predicted by the simulations (Fig. 15), due to absorption of neutrons scattered back from soil, by the snow.

13.5.4 Effect of Snow – Observation of Long-Term Seasonal Neutron Oscillations

The potential effects of snow cover on the number of neutrons of secondary cosmic rays close to the interface between lithosphere and atmosphere has been described above. If real, such effects should be responsible for a reproducible pattern of changes in seasonal neutron fluences with higher values during summer time and lower values during snowy winter time. Because the ERBSS at the UFS has been operative since 2005, the data obtained already cover a whole solar cycle. Consequently, the data can be used and any seasonal changes could be monitored for many years for the first time. More specifically, average monthly count rates obtained with the detectors of the ERBSS were calculated and, with the unfolding procedure described above, monthly neutron energy distributions were obtained. These distributions were then used and the number of neutrons was calculated by integrating the spectra over 4 energy ranges: less than 0.4 eV (“thermal neutrons”), 0.4 eV–0.1 MeV (“epithermal neutrons”), 0.1 MeV–20 MeV (“evaporation neutrons”), above 20 MeV (“cascade neutrons”). Figs. 17 (a–d) show the results (Rühm et al. 2012). Clearly, reproducible yearly oscillations are seen, which are more dominant at lower energies, and less dominant at higher energies, with almost no effect for the cascade neutrons.

In an attempt to quantify the measured oscillations, the following function was fitted to the data shown in Fig. 16 (Eq. 6):

$$y = a \cdot \sin[(2 \cdot \pi \cdot t \cdot b/365) + d] + c \cdot t + e \qquad (6)$$

The function describes a sinodial behavior which is on top of a linear increase: *a* represents the amplitude of the oscillation, *b* the period, and *c* the slope of the linear increase (which might

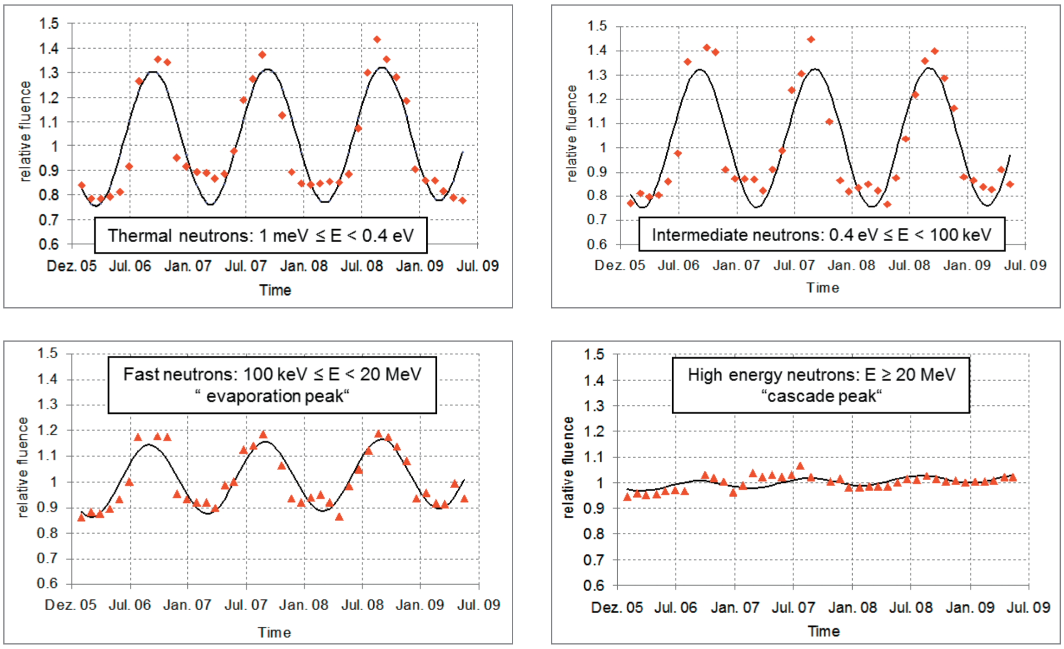

Fig. 17: Relative fluence of secondary fluences as obtained from the long-term ERBSS measurements at the UFS (closed symbols): a) thermal, b) epithermal, c) evaporation, d) cascade neutrons. Black solid line: fit through the data

be there due to the decrease in solar activity expected for the investigated period of time); d and e are additional fit parameters, t represents the time.

As a consequence of the observed oscillations, the radiation dose due to neutrons from secondary cosmic rays will also change and oscillate with time. Based on the results obtained, Fig. 18 shows the neutron doses, in terms of $H^*(10)$, at the UFS as a function of time, for the investigated period. Application of the fit function given above results in the following numerical parameters: $a = 0.068 \pm 0.006$, $b = 0.999 \pm 0.014$ und $c = (3.3 \pm 1.2) \times 10^{-5}\, d^{-1}$.

The fit parameters obtained suggest a duration of the oscillations of about 1 year (parameter *b*). The neutron dose varies between ±7 %. Finally, parameter c suggests a slight increase in neutron dose of about 1.2 % per year, due to the decrease in solar activity during the measurement periods. Interestingly, neutron monitors suggest a similar increase in count rate during this period of time. Details of these results are given in Rühm et al. 2012.

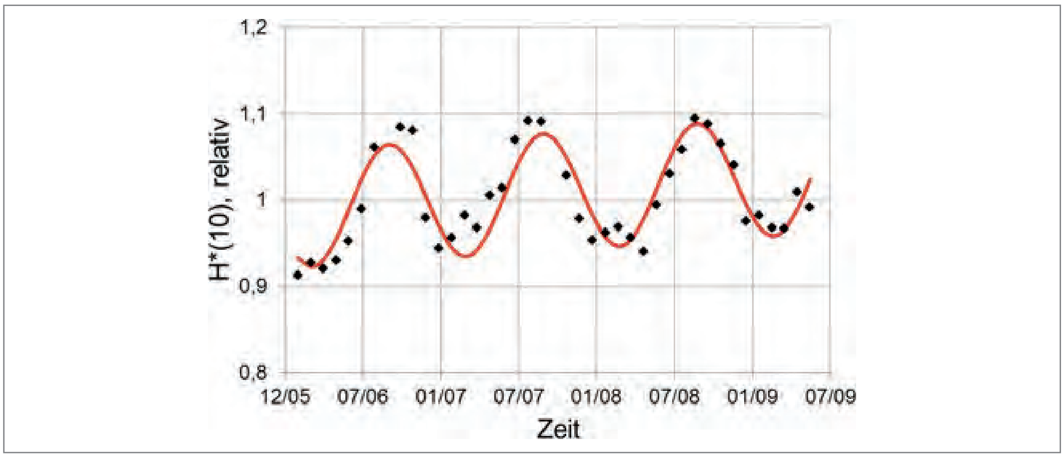

Fig. 18: Relative ambient dose equivalent from neutrons of secondary cosmic rays.

References

Alevra AV, M. Cosack, J. B. Hunt, D. J. Thomas, H. Schraube, Experimental determination of the response of four Bonner sphere sets to monoenergetic neutrons (II) Radiat. Prot. Dosim. 40, 91–10 (1992).

Bramblett, Richard L.; Ewing, Ronald I.; Bonner, T.W. (1960). "A new type of neutron spectrometer". Nuclear Instruments and Methods. **9** (1): 1–12.

Feynman, J. G. Spitale, J. Wand, and S. Gabriel, Interplanetary Proton Fluence Model, J. Geophys, Res. 98, 13281–13294 (1993).

Grieder, P. (2001) Cosmic Rays at Earth: Researcher's Reference Manual and Data Book. Elsevier, 1st edition

International Commission on Radiation Units and Measurements (1993) Quantities and Units in Radiation Protection Dosimetry. ICRU Report 51.

International Commission on Radiological Protection (2007) Recommendations of the International Commission on Radiological Protection. ICRP Publication 103, Ann. ICRP 37(2–4), Elsevier, 2007.

Leuthold G, V. Mares, W. Rühm, E. Weitzenegger, H. G. Paretzke. Long-term measurements of cosmic ray neutrons by means of a Bonner spectrometer at mountain altitudes – first results. Radiation Protection Dosimetry, Vol. 126, No. 1–4, pp. 506–511, 2007.

Mares, V., G. Schraube, H. Schraube, Calculated neutron response of a Bonner sphere spectrometer with 3He counter Nucl. Instr. Meth. A 307, 398–412 (1991).

Mares V., H. Schraube, High energy neutron spectrometry with Bonner spheres, Proceedings, The IRPA Regional Symposium on Radiation Protection in Neighbouring Countries of Central Europe, Prague, Czech Republic, September 1997, 543–547, (1998a) http://www.iaea.org/inis/collection/NCLCollectionStore/_Public/30/031/30031466.pdf

Mares, V., A. Sannikov, H. Schraube, The response functions of a 3He-Bonner spectrometer and their experimental verification in high energy neutron fields, SATIF-3 Proceedings, Sendai, Japan, 237–248 (1998b)

Mares, V., Maczka, T., Leuthold, G. Rühm, W.: Air crew dosimetry with a new version of EPCARD, Radiat. Prot. Dosim. (2009), Vol. 136, No. 4, pp. 262–266.

Mares, V., C. Pioch, W. Rühm, H. Iwase, Y. Iwamoto, M. Hagiwara, D. Satoh, H. Yashima, T. Itoga, T. Sato, Y. Nakane, H. Nakashima, Y. Sakamoto, T. Matsumoto, A. Masuda, H. Harano, J. Nishiyama, C. Theis, E. Feldbaumer, L. Jaegerhofer, A. Tamii, K. Hatanaka, T. Nakamura., Neutron dosimetry in quasi-monoenergetic fields of 244 and 387 MeV, IEEE Trans. Nucl. Sc. 60, 299–304 (2013).

Mares, V.; Rühm, W., Computerprogramme zur Dosisberechnung beim Fliegen am Beispiel von EPCARD., StrahlenschutzPRAXIS 2, 18–21 (2014).

Matzke, M. Private communication. Later Integrated into the Neutron2: Metrology File NMF-90, available from NEA Databank. http://www.nea.fr/abs/html/iaea1279.html (1987).

Matzke, M. Propagation of uncertainties in unfolding procedures. Nucl. Instrum. Methods Phys. Res. A 476, 230–241 (2002).

McElroy, W., Berg, S., Crockett, T. and Hawkins. R. Spectra Unfolding. Technical Report AFWL-TR-67-41, US Air Force Weapons Laboratory (1967).

Reginatto, M. Overview of spectral unfolding techniques and uncertainty estimation. Rad. Meas. 45, 1323–29 (2010).

Röhrs, K. (1995) The neutron monitor at Kiel (Germany) operated by the Extraterrestrial Physics Department of the Institute for Experimental and Applied Physics of the Christian-Albrechts University of Kiel.

Roesler, S., W. Heinrich, H. Schraube, Monte Carlo calculation of the radiation field at aircraft altitudes, Radit. Prot. Dosim. 98, 4, 2002, 367–388.

Rühm, W., V. Mares, C. Pioch, E. Weitzenegger, R. Vockenroth, and H. G. Paretzke (2009a), Measurements of Secondary Neutrons from Cosmic Radiation with a Bonner Sphere Spectrometer at 79°N, Radiat. Environ. Biophys., 48, 125–133.

Rühm, W., V. Mares, C. Pioch, G. Simmer, and E. Weitzenegger (2009b), Continuous measurement of secondary neutrons from cosmic radiation at mountain altitudes and close to the North Pole-A Discussion in terms of H*(10). Radiat. Prot. Dosim., 136(4), 256–261.

Rühm, W., U. Ackermann, C. Pioch, and V. Mares. Spectral neutron flux oscillations of cosmic radiation on the Earth's surface. J Geophys Res 117, A08309, 2012.

Shea, M.A. and D.F. Smart, A Summary of Major Solar Proton Events, Solar Phys. 127, 297–320 (1990)

Shea, M.A. and Smart, D.F., Cosmic Ray Implications for Human Health. Space Science Reviews, 93, 187–205 (2000).

Shea, M.A. and D.F. Smart, Patterns of Solar Proton Events over Four solar Cycles, Proc. 26th Int. Cosmic Ray Conf. 6, 374–377 (1999).

Simmer, G., Mares, V., Weitzenegger, E. and Rühm, W. Iterative unfolding for Bonner sphere spectrometers – sensitivity analysis and dose calculation. Radiat. Meas. 45, 1–9 (2010).

Thomas, DH, A.V. Alevra, J.B. Hunt, H. Schraube Experimental determination of the response of four Bonner sphere sets to thermal neutrons Radiat. Prot. Dosim. 54, 25–31 (1994).